Salvador, FJ.; Ruiz, S.; Crialesi Esposito, M.; Blanquer Espert, I. (2018). Analysis on the efects of turbulent inflow conditions on spray primary atomization in the near-field by direct numerical simulation. International Journal of Multiphase Flow. 102:49-63. https://doi.org/10.1016/j.ijmultiphaseflow.2018.01.019

Analysis on the Effects of Turbulent Inflow Conditions on Spray Primary Atomization in the Near-Field by Direct Numerical Simulation

F.J. Salvador[a,*], Ruiz, S.[a], Marco Crialesi-Esposito[a], Ignacio Blanquer[b]

[a] *CMT-Motores Térmicos, Universitat Politècnica de València, Camino de Vera, s/n, Edificio 6D 46022 Valencia, España*
[b] *Instituto de Instrumentación para Imagen Molecular (I3M). Centro Mixto CSIC– Universitat Politècnica de València–CIEMAT.*

Abstract

It is widely acknowledged that the development of sprays in the near-field is of primary importance for the spray formation downstream, as it affects both the spray angle, as well as the intact core length. In this frame, the present work aims to study the effects of turbulence inlet boundary condition on the spray formation by means of Direct Numerical Simulations on a real condition at low Reynolds number. To this extent, the code Paris-Simulator has been used, while a digital filter-based algorithm was used in order to generate synthetic turbulence at the inlet boundary condition. The influence of turbulence intensity and lengthscale on the atomization process has been studied and analyzed through 3 simulation for which these parameters have been varied. The results clearly highlight how the atomization is heavily affected by the inlet turbulence configuration. An analysis of the different atomizing conditions has been conducted, aiming to understand how the variation introduced by the inlet boundary condition on the velocity field is affecting the local atomization dynamics.

Keywords: Spray, atomization, DNS, Paris-Simulator, turbulence.

Nomenclature

$\mathbf{A}$	Correlation tensor
C	Volume fraction
$\mathbf{D}$	Deformation tensor
D	Nozzle diameter
D_l	Ligament diameter
I	Turbulent intensity
L	Turbulent lengthscale
Oh	Ohnesorge number
R	Autocorrelation function
V	Droplet volume
$\mathbf{U}$	Velocity mean component
b	Filter coefficient
d	Distance vector
d_v	Droplet volumetric diameter
m_c	Mass concentration
n	Discrete lengthscale
p	Pressure field

*Corresponding author.Tel.: +34 963879659; fax: +34 963877659.
Email addresses: fsalvado@mot.upv.es (F.J. Salvador), saruiz@mot.upv.es (Ruiz, S.), marcres@mot.upv.es (Marco Crialesi-Esposito), iblanque@dsic.upv.es (Ignacio Blanquer)

r	Random component
$r_{1/2}$	Radius of half velocity drop
u	Velocity field
u'	Velocity fluctuating component
u_τ	Shear velocity
We	Weber number
x	Spray axial direction
Greek Symbols:	
α	Gaussian coefficient
δ_s	Dirac distribution function
κ	Curvature function
λ	Ligament wavelength
μ	Dynamic viscosity
ρ	Density
σ	Surface tension
Subscript:	
g	Gas phase
l	Liquid phase

1. Introduction

Atomization process in a spray has been an important issue for researchers during last couple of decades due to its presence in many industrial applications. In fact, spray atomization is of fundamental relevance in combustion process and pollutant formation, as widely addressed in [1, 2]. As regulation on pollutant emission and energy efficiency are becoming more and more restrictive, the scientific community has invested considerable time and resources addressing the combustion process from both a theoretical and a practical standpoint, both with numerical and experimental techniques. In this context, it is nowadays evident that the actual knowledge on sprays, primary and secondary atomization as well as coalescence is far from been complete.

In this work, Direct Numerical Simulation (DNS) technique is used to provide a detailed description of the very first millimetres downstream the nozzle: this area is of fundamental importance in the formation of the spray, as it represents the regions in which the atomization begins ([3]) due to the combination of aerodynamic drag forces and air/liquid interaction. As a simulation environment, the code Paris-Simulator, developed by [4, 5], has been chosen.

The results provided up to now with DNS for the near-field region have reportedly simulated low injection velocity, therefore under pressure conditions unrealistic for Diesel ICE and rare for Gasoline Direct Injection ICE. Currently, only Lebas et al. [6] have simulated turbulence at the outlet of the nozzle, accounting for the turbulence generated by the fluid inside the nozzle duct. Many studies have related cavitating [7, 8, 9, 10, 11, 12, 13] and non-cavitating conditions [14, 15, 16, 17] inside the nozzle with non negligible effects on the turbulence distribution at the nozzle outlet. Furthermore, it has been proved in previous works [18] [19] that the higher the turbulence at the injector outlet is, the more the atomization affects the spray shape, as the intact core length reduces significantly and the atomization process starts earlier.

Various approaches have been proposed to simulate a synthetic turbulent inflow boundary condition. Klein et al. propose in [19] to use a linear-non recursive filter, based on the hypothesis of homogeneous turbulence, to filter a random signal. The result of the filtered procedure is a correlated field in both time and space. An interesting and useful modification to this procedure was provided by Hoepfner et al. in [20], where an auto-regressive procedure was used to determine the filter coefficients. This method requires an a-priori knowledge of the turbulence behavior that will be replicated by the synthetic turbulence generator, but it offers a higher flexibility in setting both the time and the lengthscale, allowing to inject vortices of different size an with different dynamic behaviour.

In [21], Perret et al. used Proper Orthogonal Decomposition (POD) to extract the turbulence coherent structures from experimental data. A non-linear Reduced Order Model is then generated using Galerkin projection, which has been widely used in CFD thanks to its capabilities to replicate the non-linear behaviour of turbulence. Still, as for [20], accurate and verified data are required in order to reproduce the injected turbulence behaviour, which may not always been available or adequate to fit the required time or space scale.

In [22], Lee et al. used a Fourier harmonics based method to reproduce the behaviour of a certain portion of the energy spectra. Each Fourier mode is individually computed and finally combined with the others through the use of a random phase. This method shows interesting results for isotropic decaying turbulence, but it is worth notice that the maximum change of the random phase and the time needed by the phase to actually change may influence the turbulence behaviour, leading to possible non-physical results [23].

Some interesting reviews of the methodologies for the generation of this synthetic turbulence (not all of them feasible for this test case) are given in [23, 20, 24]. Nevertheless, it has been proven by Druault et al. [25] that uncorrelated velocity fluctuations decays rapidly and are not able to maintain turbulence. Therefore the usage of a synthetic inlet condition correlated in time and space is mandatory to reproduce the behaviour of the nozzle outlet velocity field.

As the effects of the turbulence may only be assessed after a significant penetration, due to the required time for shear stresses to participate in generating the surface instabilities on the spray core [26], no comparison on the effects of different methodologies have been made, although it may represent an interesting analysis for future developments. Finally, the method proposed by [19] has been used, due to the promising results obtained in [6].

As appears evidently, still large improvement in the understanding of turbulent atomization can be achieved. This work investigates the effects of turbulence on the spray's shape and formation, while simulating the inlet turbulence with a methodology derived by Klein et al. [19] and applied to circular jet. In order to do so, 3 cases have been simulated with increasing inlet turbulent kinetic energy, in order to study high atomization in turbulent regimes typical of high speed jets, while minimizing the simulation domain.

2. Model Description

2.1. Governing Equations

As already stated, as a base for the fluid dynamic solver, the fixed cartesian grid eulerian-eulerian solver implemented in Paris-Simulator [27][28] was used. Under the assumption of incompressible flow for both liquid and gas (valid for Mach number lower than 0.3), the continuity equation gives a divergence free velocity field

$$\nabla \cdot \mathbf{u} = 0 \tag{1}$$

while the Navier-Stokes equation appears in its form:

$$\rho(\partial_t \mathbf{u} + \mathbf{u} \cdot \nabla \mathbf{u}) = -\nabla p + \nabla \cdot (2\mu \mathbf{D}) + \sigma \kappa \delta_s \mathbf{n} \tag{2}$$

where ρ is the fluid density, $\mathbf{u}$ is the velocity field, p is the pressure field, μ is the dynamic viscosity.

The last term on the right hand side of equation (2) represents the surface tension, for this reason a Dirac distribution function is used, namely δ_s, to concentrate this force on the liquid surface. Consequently, according to the surface tension definition, σ is the surface tension and κ is the liquid surface curvature.

The term $\mathbf{D}$ represents the deformation tensor, expressed as:

$$\mathbf{D} = \frac{\partial_i u_j + \partial_j u_i}{2} \tag{3}$$

In this work, the one-fluid method is used to compute the local value of density and viscosity. According to this methodology, an advection equation for the volume fraction C is implemented as:

$$\partial_t C + u \cdot \nabla C = 0 \tag{4}$$

therefore, the local properties are calculated through an arithmetic mean, as:

$$\begin{aligned} \rho &= C\rho_l + (1-C)\rho_g \\ \mu &= C\mu_l + (1-C)\mu_g \end{aligned} \tag{5}$$

Where the subscripts l and g indicate respectively the liquid and the gas phase. The solution of the governing equation is given using the Chorin projection method [29], a second-order accurate predictor-corrector time scheme is used [28], while a third-order QUICK scheme for the time discretization is implemented [30]. Finally the advection equation for the color function is solved through the Volume of Fluid (VOF) method [31]. Further details on the solver and the numerical solution may be found in [28, 4].

2.2. Synthetic Turbulence Boundary Condition

As already stated in section 1, the simulation of a inlet turbulence condition for the jet is of fundamental importance to reproduce the real behaviour of atomization. In this work, the simulation domain is box-shaped with cubical cells (according to the solver configurations [4]), with a circular spray incoming from the $-\hat{x}$ direction, with a positive velocity component in the $\hat{x}$ direction. In this frame, the turbulence have to take into account the following features:

- the turbulence has to be distributed on all of the velocity components, with a pre-determined velocity module.
- the turbulence has to be zero-mean in time on all the components, so that the resulting mean component is the original and stationary velocity field input.
- the turbulence distribution has to be continuous in time and space, at all time steps.

To accommodate all this necessities, the original algorithm implemented by Klein et al. [19] has been chosen as a methodology. This method already showed its capabilities for both planar [19] and circular [6] jets, although no analysis on the physical consequences of the tunable parameters of this method have been found in literature.

This method is based on the Reynolds decomposition [32] on the inlet velocity field:

$$\mathbf{u}(x_0, t) = \mathbf{U}(x_0) + \mathbf{u}'(x_0, t) \tag{6}$$

where the effective velocity $\mathbf{u}$ is decomposed into a mean field $\mathbf{U}$ and a fluctuating component $\mathbf{u}'$ that is based on a random component. This kind of decomposition for the inlet boundary condition allows to model the behavior of u', so that a one point correlation can be imposed, as well as a limitation on the energy level associated with the fluctuating component. In order to determine the fluctuation, it might be decomposed into the product of two factors, namely the Reynold stress tensor and random velocity field, continuous in time and space. Consequently, equation (6) can be rewritten as:

$$\mathbf{u}(x_0, t) = \mathbf{U}(x_0) + \mathbf{A} \cdot \mathbf{u}'(x_0, t) \tag{7}$$

$\mathbf{A}$ is a correlation tensor of coefficients a_{ij}, that is designed to match the desired Reynold Stress Tensor from equation (7), as demonstrated in [33]. The non-zero Tensor components are:

$$\begin{aligned} a_{11} &= \sqrt{R_{11}}, \\ a_{21} &= R_{11}/a_{11}, \\ a_{22} &= \sqrt{R_{22} - {a_{21}}^2}, \\ a_{31} &= R_{31}/a_{11}, \\ a_{32} &= R_{32} - a_{21}a_{31}/a_{22} \\ a_{33} &= \sqrt{R_{33} - {a_{31}}^2 - {a_{32}}^2}. \end{aligned} \tag{8}$$

Where R is the autocorrelation function, that may be obtained from internal nozzle flow simulations. In order to determine the fluctuating component, a linear non-recursive Finite Impulse Response (FIR) filtering procedure is applied to a random field, as:

$$u' = \sum_{n=-N}^{N} b_n r_{n+m} \tag{9}$$

where r is the random field and b_n are the filter coefficients. While the determination of r is a straight forward procedure, it is important to have $\bar{r}_m = 0$ and $\overline{r_m r_m} = 1$ in order to obtain a two-point correlation.

The determination of the filter coefficients, can be derived through the definition of the autocorrelation function of equation (9) as:

$$\frac{\overline{u'_m u'_{m+k}}}{\overline{u'_m u'_m}} = \frac{\sum_{j=-N+k}^{N} b_j b_{j-k}}{\sum_{j=-N}^{N} b_j^2}. \tag{10}$$

Once the statistical properties of the random field are matched, equation (10) can be used to find the filter coefficient values if an autocorrelation function (equation (10) left-hand side) is given; to overcome this obstacle, Klein et al. [19] proposed to use the 1D spatial autocorrelation provided by Batchelor in [34]:

$$R_{uu}(d,0,0) = \frac{\overline{u'_m u'_{m+k}}}{\overline{u'_m u'_m}} = exp\left(-\frac{\pi d^2}{4L^2}\right) \tag{11}$$

where d is the distance vector (characteristic of the specific problem) and L is the turbulent length scale, for which specific values may be found in [6] for cylindrical jet applications. Equation (11) can be combined with (10) and solved for b_j, obtaining

$$b_k = g_k \Big/ \sum_{j=-N}^{N} g_j^2 \quad \text{and} \quad g_i := exp\left(-\frac{\pi k}{2n^2}\right) \tag{12}$$

where $n = L/\Delta x$ is the discrete length scale (with Δx being the mesh size, uniform in the three directions in the present study).

The filtering operation can be easily convoluted in three dimensions and need no further explanations (more details and suggestion on the filter implementation can be found in [19]).

2.3. Velocity Inlet Profile and Turbulence Distribution

The usual approach in DNS simulations of sprays [3, 6, 18] is to use a flat-top inlet velocity profile, as the actual profile developed inside the injector is still being discussed and strongly depends on the injector geometry. Therefore, as many applications in different sectors (automotive, energy, aerospace, industrial) have different injection system, it is reasonable to use a fully developed turbulent pipe flow as turbulent source for the spray. In this work a turbulent pipe profile have been used both for the radial distribution of the velocity, as well as for the turbulence distribution. Many works are available on both experimental and numerical studies of pipe flow turbulence at moderate Reynolds number [35, 36]. If the mass flow rate is fixed, the mean velocity profile $\mathbf{U}(x_0)$ impose a significantly higher velocity at the centerline for the case accounting for the wall effects as compared to a typical flat-top profile. For this reason, although the bulk Reynolds Re_b remains constant in the two cases, the centerline Reynolds Re_c change significantly. Figure 1(a) shows in blue the velocity profile used in this paper, derived by the work of [35], in red the linear region ($y^+ = y^+$), while in dashed black the logarithmic region, defined by:

$$U^+ = \frac{1}{k}\log(y^+) + B \tag{13}$$

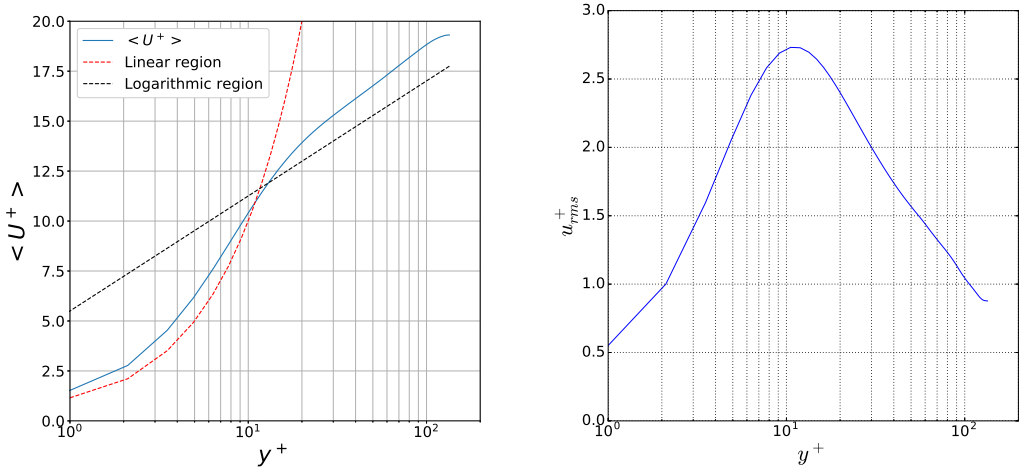

(a) Axial velocity profile in a turbulent pipe

(b) Axial velocity fluctuation profile in a turbulent pipe

Figure 1: Turbulent pipe velocity profile, from [35].

with $k = 0.4$ and $B = 5.5$. The y^+ is defined as:

$$y^+ = \frac{y u_\tau}{\nu} \tag{14}$$

where y is the wall distance, u_τ is the shear velocity and ν is the kinematic viscosity.

The fluctuating velocity component $(u'(x_0, t))$ distribution has been set so that it will comply with the behaviour illustrated in Figure 1(b).

3. Cases of Study

The main objective of this work is to provide an insight on the primary atomization in the early spray formation region, usually quantifiable in high speed sprays between $2 - 3$ mm of distance from the orifice. In this region many types of atomization occur, starting from the mushroom tip breakup, followed by atomization induced by the aerodynamic forces on the spray core.

Very few experimental works are available on near field visualization [37, 38, 39, 40]; furthermore to the best of the authors knowledge, none at low speed (corresponding to low injection pressures), which is mandatory for DNS simulations. For this reason, the liquid/gas parameters, as well as the geometrical parameters were chosen according to a Spray A usual configuration [41], where a low speed Dodecane jet is injected in a pressurized nitrogen vessel. Experiments on Spray A case have been conducted extensively throughout last years and it is likely to be the best experimental configuration for future validation of simulation results. The parameters used are resumed in Table 1.

As known from the theory of self-similarity in sprays and jets [32], the velocity profile assumes a gaussian shape only for $x/D > 25 \div 30$, where x is the spray axial penetration and D the nozzle diameter. In order to comply with this hypothesis, the turbulence inside the nozzle needs to be simulated and used as a boundary condition in the DNS simulation , in order to prompt the atomization process and therefore leading to a axial breakup that will ultimately allow to generate a gaussian profile. This consideration also guides in the design of the simulation domain. In order to replicate and verify this behaviour, the domain has been set to 2.34 mm, 0.6 mm 0.6 mm in x, y and z respectively. As suggested in [42] the cells are cubes of 2.34 μm, resulting in approximately 65.5 millions of cells.

Parameter	Values	Units
Injector diameter	0.09	mm
Fuel viscosity	$1.34 \cdot 10^{-3}$	$Pa \cdot s$
Fuel density	750	kg/m^3
Fuel Mean Velocity	100	m/s
Fuel/Nitrogen Surface Tension	$2.535 \cdot 10^{-2}$	N/m
Nitrogen Viscosity	$1.85 \cdot 10^{-5}$	$Pa \cdot s$
Nitrogen Density	22.8	kg/m^3

Table 1: Simulation physical parameters

As reported in [6], the turbulent length (L) scale can be assumed as 10% of the diameter and the turbulent intensity (I) might be assumed as a 5% of the axial mean velocity. Still, the turbulent length scale may change significantly with the nozzle geometry: for this reason, one of the main goal of this work is to assess the effects on the primary atomization of the parameter L by means of 3 DNS cases, described in table 2.

	L	Re_c	Re_b
case 0	0	5037	5037
case 1	$0.1D$	6700	5037
case 2	$0.17D$	6700	5037

Table 2: Inlet turbulence model parameters for all the cases simulated

As far as the author's knowledge goes, no previous researches on the topic are available where L have been investigated by a parametric study. Furthermore, as most studies on internal nozzle presents velocity fluctuations that are comparable to the one used here, the main effort is concentrated on the lengthscale L. The parameter L acts directly as a source for turbulent energy for the spray. In fact, the formation of larger turbulent structures, such as eddies and vortices, generates a cascade effect that distributes the energy to the lower scales. As it will be shown in section 4.4, the local atomization is highly influenced by the wavelength of the local disturbances, therefore the L parameter is a key factor in determine the droplet breakup regime.

4. Results and Discussions

In the present section, first a comparison of the three cases will be made in section 4.1 aiming to highlight the differences introduced by the different boundary conditions depicted in Table 2. Section 4.2 will focus the analysis on the spray morphology, while section 4.3 will discuss the effects of the different axial velocities in the 3 cases. The analysis of the physical processes generating the atomization will be addressed in section 4.4. The droplet analysis, in terms of diameter, distribution and physical properties will be studied in section 4.5. Finally, some considerations on the basic properties of the gaussian profile has been made in section 4.6.

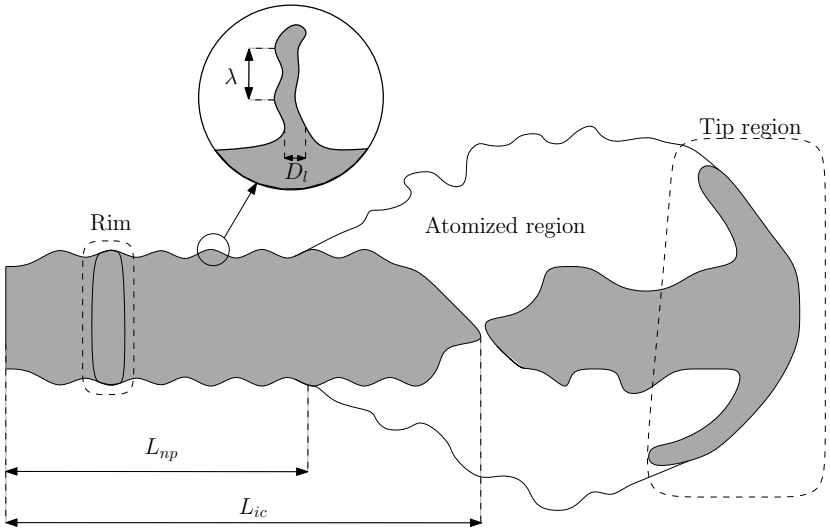

Figure 2: Schematic representation of the spray, presenting the nomenclature used in the analysis.

Figure 2 shows a schematic representation of the main spray elements analysed in this paper. The *external non-perturbed length*, L_{np}, coincides with the length of the spray region where the liquid core maintains a pseudo-cylindrical shape, before the *atomized region*. The *intact core length*, L_{ic}, is the statistical length that determines the distance between the injector nozzle outlet and the point in the spray axis in which the probability of finding liquid is below 99.9% (hence the axial liquid column stop being continuous). The ligaments will be identified by their diameter, D_l, and their external perturbations will be described by the wavelength, λ, that the liquid interface forms due to external disturbances. As the spray starts atomizing, an *atomized region* is formed, where the spray core is hidden by the droplets cloud. This droplets cloud is usually used to define the spray cone angle in near-field visualization experiments. The *tip region* is the region where the cylinder spray is bent by its impact with calm air. Finally, the irregularity created on the external liquid core (visible in the *external non-perturbed region*) are called *rims*. This liquid structures are of fundamental importance as they are directly involved in the ligaments formation.

4.1. Effects of the Synthetic Boundary Conditions

As a first validation of the methodology, Figure 3 highlights the changes generated by the synthetic turbulence boundary condition, presented in section 2.2 for the 3 cases (Table 2). This figure shows the vorticity effects generated by the inlet turbulence on the liquid surface (here represented with VOF isosurface) over the spray *external non perturbed region* at $t = 20\ \mu s$.

Figure 3(a) shows the vorticity field on a 2D section. The synthetic turbulence in case 0 to 2 increases the area influenced by a strong vorticity field, as already observed in section 3; in particular is clear how cases 1 and 2 present a strong turbulent field and how the area of influence of the turbulent structures grows with the parameter L. Figure 3(a) highlights how, for higher values of L, the structures generated within the spray in the *external non perturbed region* increase their size, the region of influence and their magnitude. It is notable that in case 2, the structures reaches the fluid surface faster than in case 1, leading to consequent larger portions of the liquid core been affected by irregularities, as shown in Figure 3(b). On the other hand, case 0 shows a plane aspect, leading to the conclusions that in this region of the spray the aerodynamic forces are not sufficient to generate perturbation on the liquid surface. This behaviour observed in case 0 lead to an atomization process almost only exclusively promoted by the spray tip breakup.

Figure 4 shows, in the upper part of the spray, a scheme of the eddies formation, while in the lower part the air relative velocity with respect to the spray. This simple scheme can help to explain the three different effects generated by the turbulent inlet condition on the atomization process, which are described in the following:

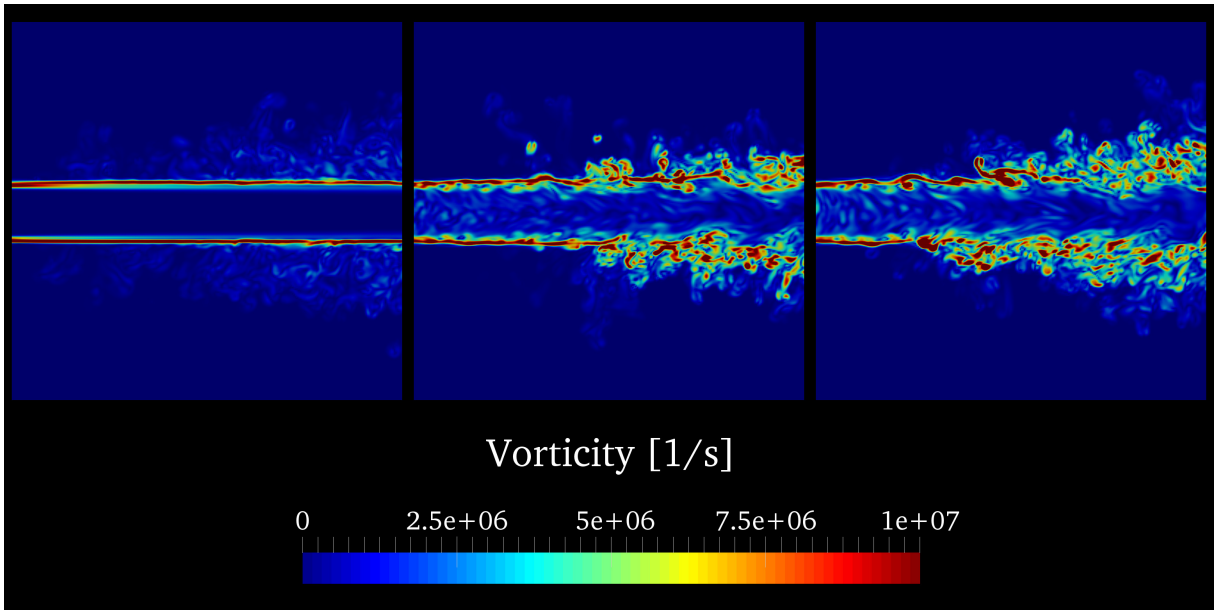

(a) Vorticity in the spray core in the external non perturbed region. Left to right case 0, 1 and 2.

(b) VOF renderization in the external non perturbed region.

Figure 3: Spray behavior in the transient spray under the sinthetic boundary condition effects. Left to right case 0, 1 and 2.

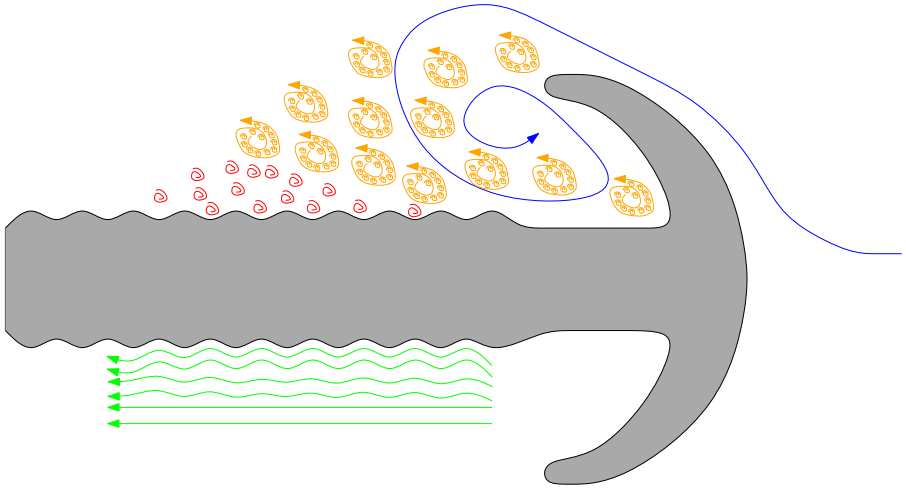

Figure 4: Simplified scheme of the distribution of aerodynamic drag forces and vorticity field around the spray tip and core

(1) The synthetic turbulence described in section 2.2 generates effects in the three dimensions and deforms the liquid core from the inside-out. The velocity propagation in the core, allows the formation of rims of small size along the liquid core in the first milliseconds of the spray penetration.

(2) The tip bends due to its impact with calm air, generating the mushroom shape peculiar of the *tip region*. This liquid-gas interaction generates, at first, an eddy structure of large size (even larger than the nozzle diameter), represented as a single blue line in Figure 4. This large turbulence structure is a toroid in three dimensions. The large eddy contributes to both modify and perturb the liquid region below the spray tip. While doing so, the structure decomposes into smaller eddies that propagates in the opposite direction with respect to the spray penetration (the yellow and red structures in Figure 4). As this smaller eddies are moving from the *tip region* towards the liquid core, they acts as external disturbance for the core liquid surface, while amplifying the rim size and modifying the local velocity field, eventually leading to the core breakup (defined by the *intact core length*).

(3) As the spray keeps penetrating, the effects of the vortex cascade generated by the larger tip eddy are mitigated, due to the higher distance a eddy has to travel to reach the nozzle outlet. As a matter of facts, the vorticity effects on the spray core almost disappear after a certain spray penetration. Once this level of penetration has been reached, the only force acting on liquid core is the aerodynamic drag force. As a well known phenomena, the drag depends on the relative velocity between the two moving bodies or, in this case, between the two phases as showed in Figure 4 with green lines. When a rim is formed (by the mechanism depicted in (1) without the contribution of the effects explained in (2)) the green line in Figure 4 are bended and the drag forces generate a radial stress that acts like a disturbance. This radial disturbance is way more important in the spray core deformation than the simple axial stress generated in absence of rims.

Figure 5 shows a 2D section of the simulation domain for case 0 (top) and case 1 (bottom). The liquid phase is represented and the field is coloured by the vorticity field; finally, are displayed on the background vortex lines obtained from the Line Integral Convolution (LIC) technique are displayed. The comparison is made at 10 μs after injection starts. Here the hypothesis (1), (2) (3) on how the velocity fields develops and affects the atomization process can be numerically observed. At this time, the spray penetration is still reduced (when compared to the whole domain) but it is quite evident the difference that effects (2) and (3) are inducing on the spray core and on the atomization process (especially for case 0). Furthermore, at this instant, case 1 is still showing an almost intact liquid core, which make easier to apply the analysis of the effects (2) and (3).

In a first place, the turbulence macro-structures developed in case 0 and case 1 will be analyzed, with the objective of drawing considerations on how dynamics involved with effect (2) are affected by the use of the synthetic turbulence at the inlet. In both cases, in Figure 5, the larger eddy (described in effect (2) and represented with a blue line in Figure 4) can be clearly identified by the the vortex lines around the spray tip, bended toward the spray axis. Also, the larger structure shows the same size, although case 1 display a more chaotic behaviour, obviously related to the synthetic inlet boundary conditions. This first observation lead to the conclusion that the synthetic inlet turbulence does not affect the large scale motion of the fluid (except for the spray penetration, that will be addressed later in section 4.3) as it is expected. Nevertheless, Figure 5 shows a significant variation in both the vorticity field, as well as in the shape of the liquid spray. Case 0 shows a high intensity region for vorticity only in the immediate proximity of the spray tip, suggesting how the development of turbulence in this case is strictly related to effect (2), confirming that effect (3) is still not affecting at this stage of the penetration. On the other hand, case 1 displays many dispersed high vorticity regions: in this case a more intense turbulence is generated close to the surface instability. This phenomena could be explained by the higher shear stress generated by the relative motion of liquid and gas when the liquid surface is bended and not cylindrical (as for case 0). For this reason, case 1 promote, in a first place, the generation of a more intense turbulence field around the spray.

Further observations could be made on how the instabilities are generated in the *external non-perturbed length* region. At this time, the spray is sufficiently far from the nozzle so that the effects that mechanism (2) is generating are mitigated and only effects (3) and (1) (for case 1) are responsible for the spray core perturbation in the area closer to the nozzle outlet. As showed clearly in Figure 5, case 0 shows a very cylindrical aspect in the first part (closer to the nozzle) while the liquid core got perturbed closer to the spray tip (due to effect (2)). Again, in both cases a higher values of vorticity can be observed close to the surface corrugation, while the highest vorticity value can be located close to the larger eddy's center. An insight on how the turbulence behaviour relates to the surface corrugations is given in Figure 6. This figure shows, for both, case 0 and 1, the contour of the second invariant of the velocity gradient tensor, representing hairpin vortices. Both, in case 0 and 1, a significant amount of hairpins are generated close to the spray tip. In order to isolate the effects of the synthetic turbulence, the behaviour of the vortices will be first studied for case 0, where only effect (2) is responsible for the generation of turbulent structures. Similarly to the literature results [3, 43], case 0 displays the ongoing formation of axisymmetric structure in the spray tip, normal to the penetration axis. As the spray tip penetrates, these vortices are distorted by the velocity field behind the tip. The vortices are re-oriented and finally, when they are sufficiently far from the tip, they are almost parallel to the penetration axis. The absence of structures in the region close to the nozzle suggests that, in lack of a highly turbulent environment, the vortices quickly dissipate. Case 1 displays some major differences when compared to case 0. As the synthetic inlet turbulence is imposing a fluctuating velocity in the three directions, the spray tip will display a strongly asymmetric tip when compared to case 0 (see Figure 5). Therefore, the dispersion of the turbulent structures will have a stronger radial component, while their formation will not be as axisymmetric as for case 0. Furthermore, the presence of corrugation on the spray surface in the *external non perturbed length*, due to the radial components of the injected turbulence, promote the generation of rims (effect (1)) that, due to the shear with the gas phase cause the generation of turbulence structures. This structures are similar to *horseshoe hairpin*, and ensure the conservation of the turbulence even where the disturbance generated by the spray tip cannot reach the liquid core. In other words, in case 0 the vortexes spreading from (2) are not able to reach the nozzle outlet, meaning that, for case 0, only effect (3) is acting on the spray liquid core at the immediate nozzle outlet. On the other hand, case 1 shows a significantly perturbed liquid core region, given by a mix of effects (1) and (3) explicated above. Consequently for case 0, in Figure 5 the liquid surface is perturbed only in the areas where hairpins can be found in Figure 6

Finally, the liquid core in the tip region shows a more chaotic structure and a first discontinuity in the axial mass concentration appears. The sequence of events (1) (2) (3) in case 1 generates a more severe perturbation on the liquid surface that ultimately leads to the axial breakup as the spray penetrates. Even when the liquid surface instabilities generated by (2) are far from the nozzle, effect (1) is still sustaining and even amplifying the rims in this region, increasing the aerodynamic stress generated by effect (3). Once again, the axial breakup helps interpreting the results, quantifying that the generation of rims and,

consequently, of radial forces is way more significant in the spray formation than axial shear stress induced by aerodynamic interaction between calm air and liquid.

4.2. Observation on the Spray Morphology

Figure 7 shows the external aspect of the spray at $t = 20\ \mu s$. As it can be clearly noted, the higher the turbulence induced, the sooner the atomization process starts, shortening the *external non-perturbed length*. When comparing all cases, case 2 displays the formation of a earlier *atomization region*, due to the rims created in the *external non-perturbed legth* region that creates a dense cloud of droplets in the near-nozzle field. On the other hand, it is evident that in case 0 the *external non-perturbed length* maintain an almost exact cylindrical shape up to the spray tip, due to the low nitrogen density and the low injection velocity. As a confirmation of the synthetic turbulence influence on the atomization process, in case 1 the droplet cloud (that will eventually define the spray angle) starts in an axial position between case 0 and case 2. Similar results have been obtained in [44] for a nozzle of similar size in different injection conditions.

The different behavior among the three cases can be quantified by means of the liquid mass concentration in the axis, calculated as :

$$m_c = \frac{\rho_l \cdot C}{\rho_l \cdot C + \rho_g \cdot (1 - C)} \tag{15}$$

Figure 8 shows the time-averaged mass concentration in the spray axis. Once the spray is stabilized for the three cases, m_c is used to characterized the intact core length (Figure 2), which is directly related to the atomization intensity. As it can be seen in Figure 8, in the case 0, due to the poor atomization, the mass concentration in the axis is not perturbed, showing a value of 1 (pure liquid) in the spatial window analysed (up to 2.34 mm). However, in case 1 and especially in case 2, the intact core length drastically decreases as a result of the higher turbulence induced in the nozzle exit. This behaviour quantifies the earlier qualitative explanation of Figure 7, where the *external non-perturbed length* increases with the inlet turbulence lengthscale.

It is interesting to notice that the case with the highest turbulence level (namely case 2) in Figure 3 experiences a core deformation that creates rims very close to the nozzle outlet. This generates an increase in the vorticity and in the local velocity field at the interphase between liquid and air (Figure 3(a)), finally increasing the atomization, as showed in Figure 7. The rims are almost non existent in case 0 leading to a low vorticity field and, consequently low atomization, mainly focused in this case around the spray tip where droplets are separating from the ligaments.

Finally, Figure 8 allows to estimate the liquid core length. Taking as a threshold an axial mass concentration of 0.97, case 1 and 2 present a liquid core length of $1,47\ mm$ and $1.91\ mm$ respectively, while this parameter cannot be assessed for case 0

4.3. Consideration on the Axial Spray Penetration

The results presented in Figure 7 highlights an interesting aspect about penetration, as the 3 cases seem to show different axial position of the spray tip at the same timestep. A first remark between case 0 and cases 1 and 2 involved the axial Reynolds (Re_c): as reported in Table 2, although the 3 cases have the same inlet mass flow rate (same average spray velocity at the nozzle outlet), the velocity distribution drastically changes as showed in Figure 1. Therefore, it is assumable that axial penetration is mostly a function of Re_c.

Finally, the difference in penetration between case 1 and 2 can be found in the different rate of atomization between the two cases. As showed in Figure 8, case 2 atomizes more than case 1, causing a more atomized tip region as well. This behaviour is actually responsible for the difference showed in the render in Figure 7, as the total momentum needs to be conserved. In fact it has been widely proven in sprays that the largest the angle (and therefore the spray atomization) the lower the penetration will be.

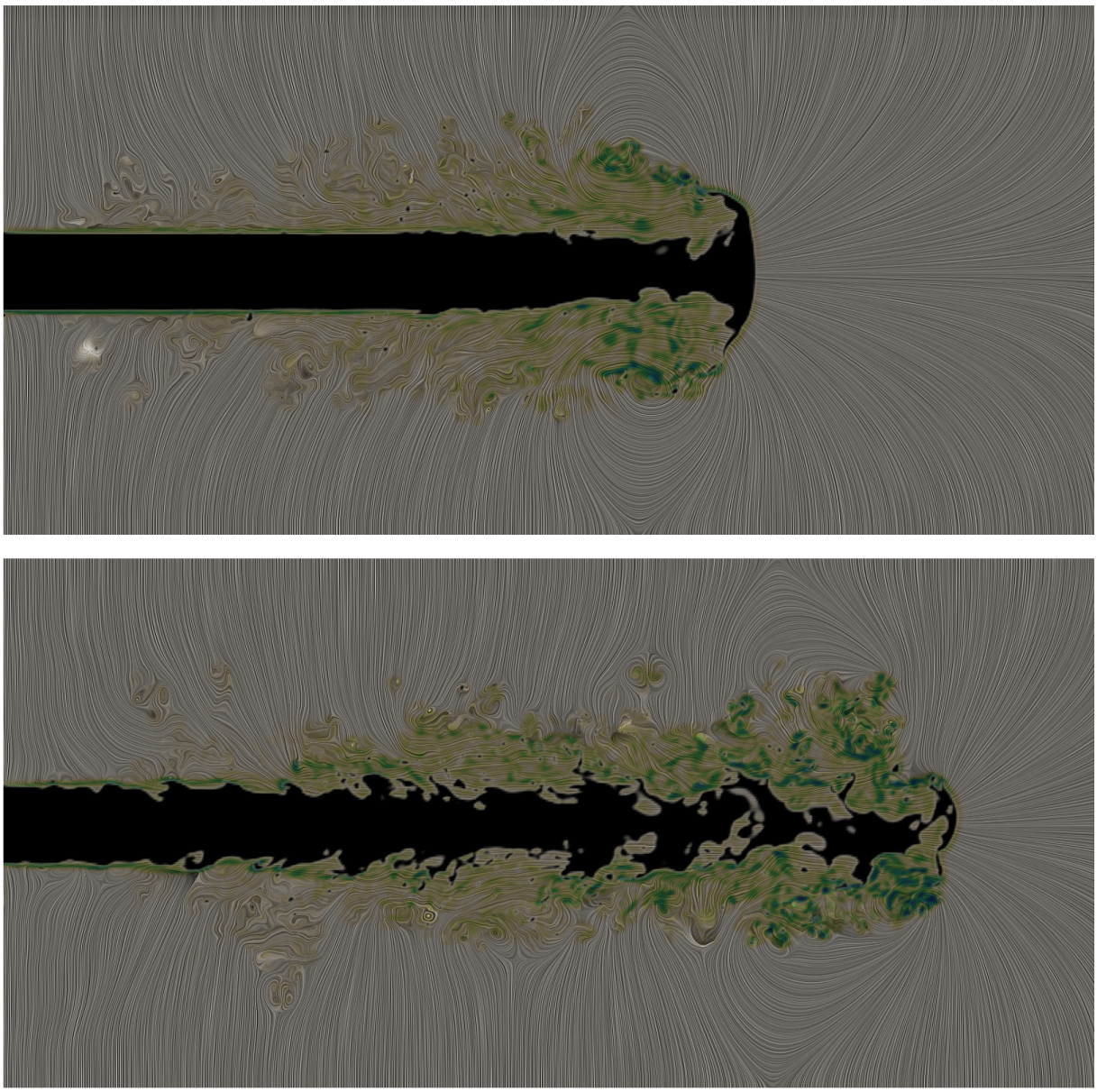

Figure 5: Case 0 and 1 at $10\mu s$.

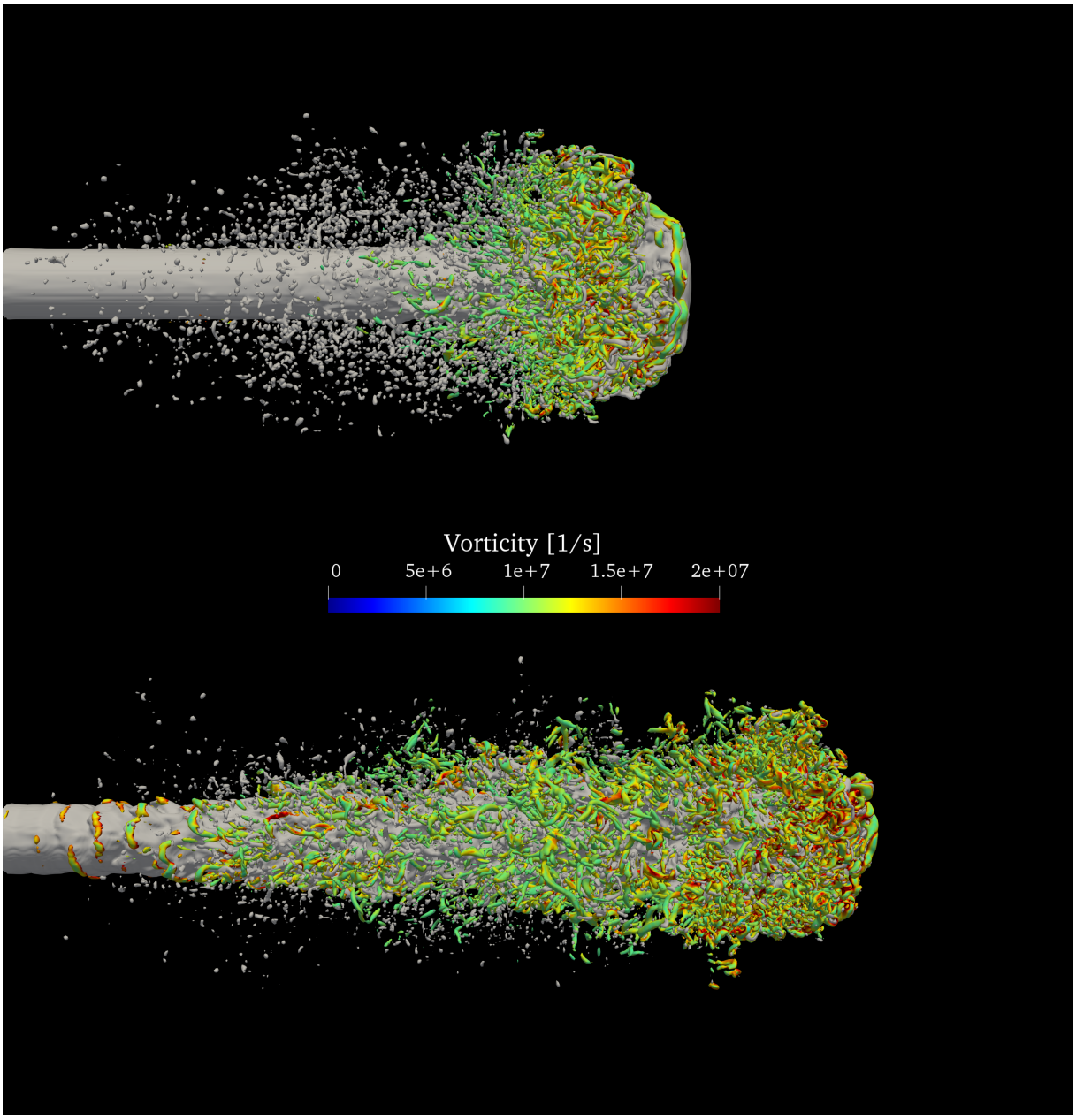

Figure 6: Turbulent structures detected through the Q-criterion for cases 0 and 1 at $10\mu s$.

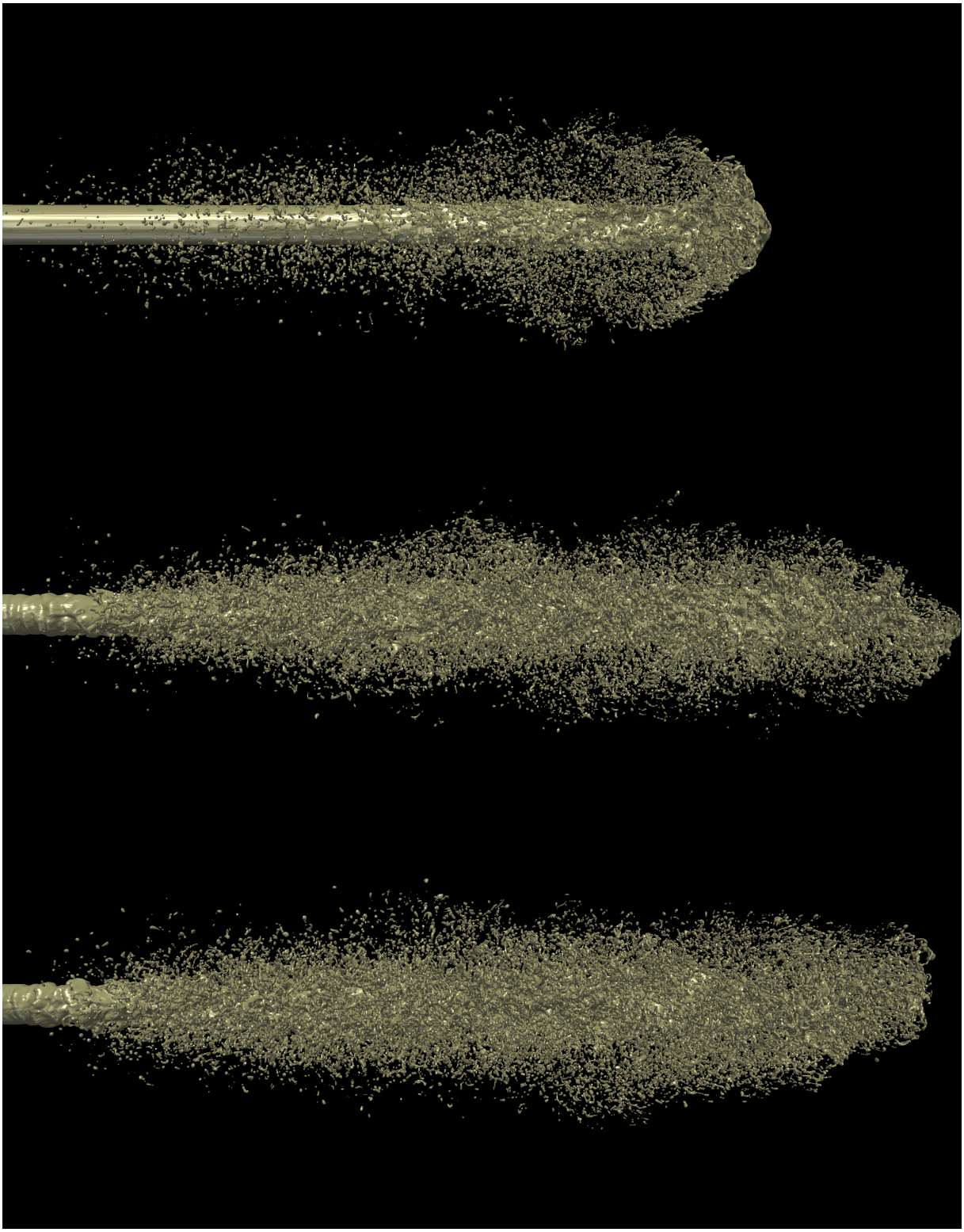

Figure 7: External aspect of the injected spray at $t = 20\mu s$. From top to bottom, case 0, 1 and 2

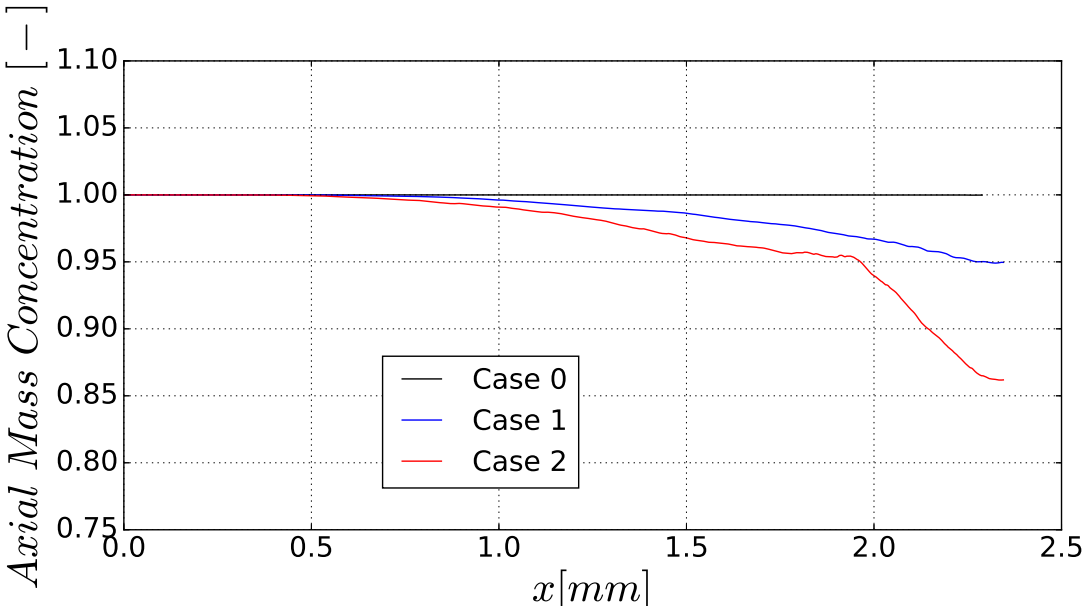

Figure 8: Axial time-averaged mass concentration

4.4. Observations on the atomization process

Shinjo et al. [3, 43] highlight how the ligaments formation could occur as a consequence of a liquid detachment from the *tip region* or from the liquid core. In the first case, the ligament are created by the shear generated by the *tip region* macro-vortex (blue line in Figure 4), while in the second scenario, the ligaments formation is related to the aerodynamic force (effect (3)), increased by the smaller eddies generated from the macro vortex (effect (2)). The analysis in [3] also highlights how one of the most significant dynamic in spray atomization is given by droplets impacting the rim surface, due to the large eddy produced by the spray tip that drove the droplets towards the spray core. A significant insight on this mechanism is given by Jarrahbashi et al. in [26]. Here the authors highlights how the shear stress, described in [45], is itself sufficient to generate counter-rotating hairpins that are responsible for the formation of ligaments and, subsequently for the primary atomization.

Figure 9 shows a zoomed view of the isolated spray core in the *external non-perturbed length region*. The vortex lines projected over the spray core are displayed in black. Finally, in analogy with [26], the vortex line belonging to the same rim are coloured in red. Figure 9 clearly displays a more chaotic surface than the one displayed in [26], nevertheless, the presence of counter-rotating vortices is evident in the red lines and, in general, along the whole region. On the other hand, assume that the rim tear (that ultimately leads to the formation of ligaments) is only due to the aerodynamic shear stress is somehow hard to prove in the three cases tested in the present work. Referring to Figure 7, is clear that the aerodynamic forces have not yet generated a sufficient tension on the liquid surface to trigger the formation of instabilities (similar results have been found in [3]).The real phenomena occurs in such a way that the *external non-perturbed length* is not able to keep the cylindrical shape for such a length as in case 0 or in [3, 43], rather it shows a behaviour closer to the one in cases 1 and 2, as showed in [46], due to the obvious perturbation that the fluid undergoes at the nozzle exit. For these reason, the rim/ligaments breakup is more likely to occur due to the combination of aerodynamic shear stress and instabilities, that may be triggered both by small vortices or by the impact of the droplets recirculated by the main larger eddy. In any case, in such a complex scenario, is difficult to separate effects, therefore future studies on this subjects are required.

Figure 10 displays the evolution of the spray in a 1 μs interval for case 1. Four zones can be can be identified, depending of the values the axial mass concentration showed in Figure 8. Obviously, the division in areas will change for each case, depending on his axial mass concentration. On the left side of the red line,

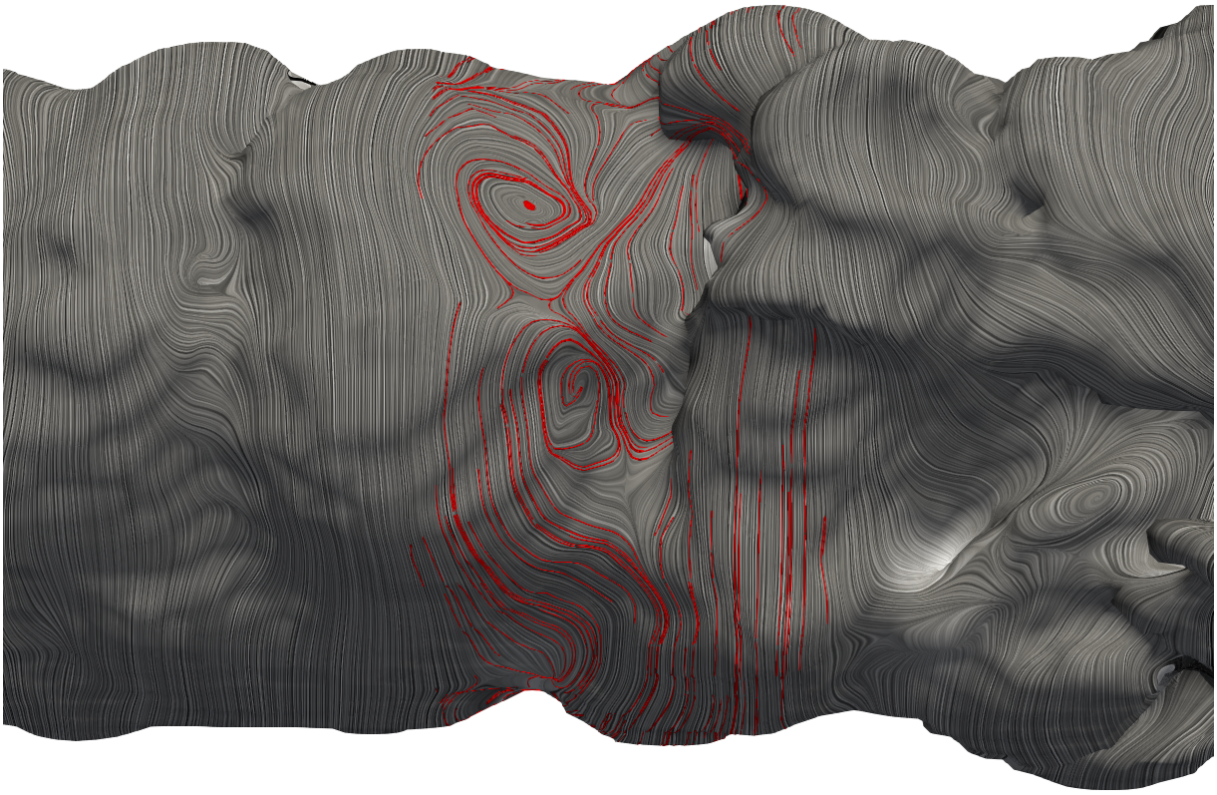

Figure 9: Detailed view of the vortex lines over the spray core at $t = 65\mu s$. In red, the vortex lines belonging to the same rim are highlighted.

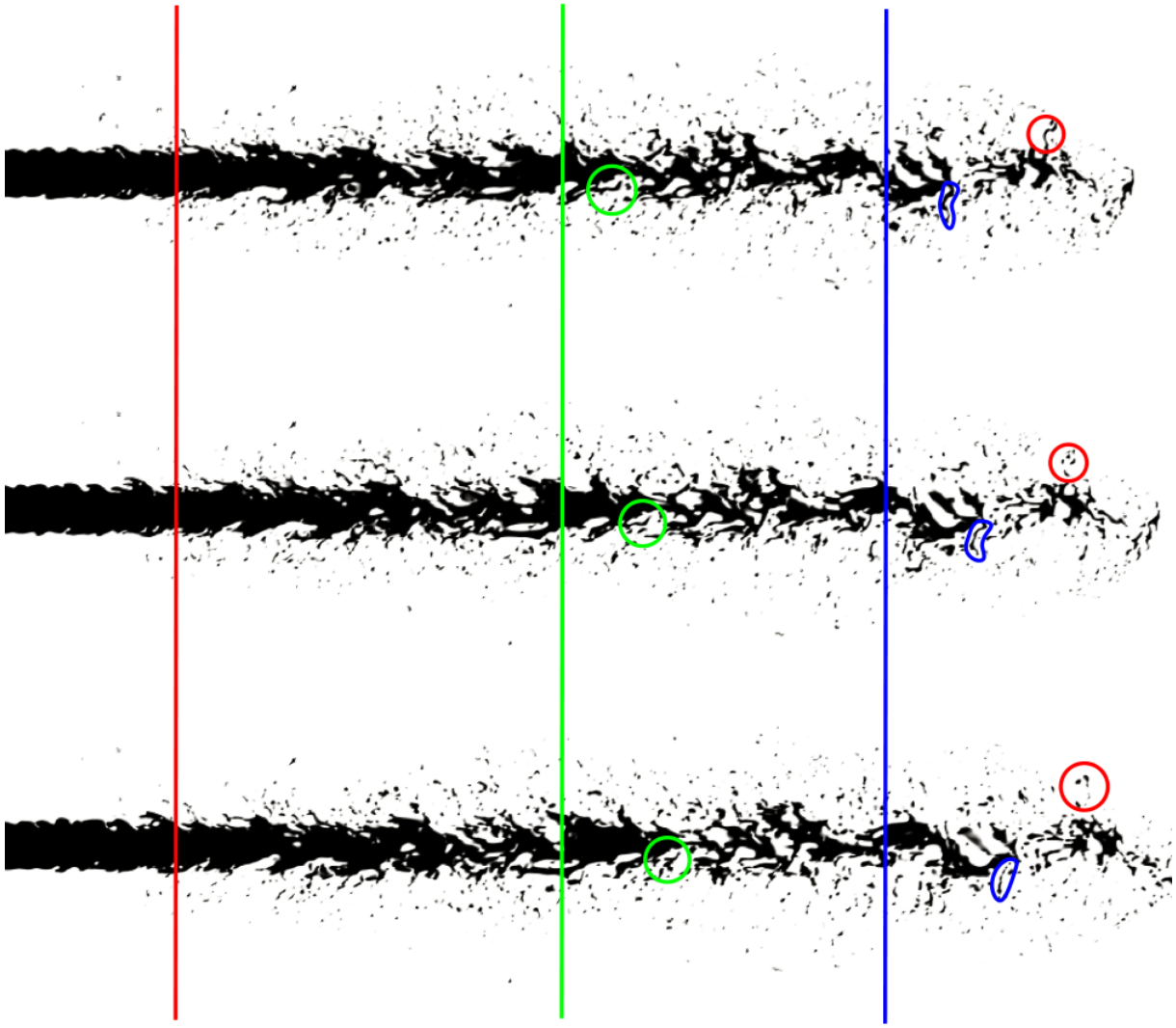

Figure 10: Time sequence of spray formation. The three planes show the liquid evolution at $20\mu s$, $20.5\mu s$ and $21\mu s$ (respectively from top to bottom) for case 1.

the *external non-perturbed length* can be identified. In this zone no major effect of the aerodynamic drag can be identified (effect (3) in section 4.1) and the external shape of the liquid core is almost uniquely affected by the inlet velocity profile (effect (1) in section 4.1). This region do not show any significant ligament and therefore no atomization is observed here; such a peculiarity is easy to observe experimentally. In fact, is one of the few measurable parameter from optical measurements [40].

A second region can be observed between the red and the green line (where the axial mass concentration drops below 99% in Figure 8). Here the small *rims* created in the previous region grow due to the increase in the aerodynamic forces acting on the spray core (effect (3) in section 4.1). This zone represents the region where atomization eventually starts and marks the border between the *external non-perturbed length* and the atomization region. As a matter of fact, some of the rims are already showing an atomized behaviour, due the ligaments created by the shear stress. Furthermore, the almost toroid/conical shape that the rims displays in the previous region is almost entirely lost here and a severe breakup has already start to occur. As can will be observed in section 4.2, this region shape depends on the turbulence intensity.

A third region, between the green and the blue line, shows a region with developed atomization regimes.

The limits of this region are given, on the left side, by the amplification of the wave amplitude of the instabilities generating the rims, while on the right side by the axial point on which the axial mass concentration drops below 97% in Figure 8. Here the atomization regime is fully developed and air-liquid interaction creates a sufficient condition to continuously support the formation of the ligaments and their instabilities, that finally determines atomization.

Finally, a last region can be analysed on the right side of the blue line. Here the axial mass concentration on time averaged results is clearly below 96% (as well as the probability to find liquid in the spray axis) and the whole movement of the liquid parts occur on larger length scales. The main liquid perturbation is given by the spray tip-air interaction. The eddies appear at a bigger scale (for the biggest reaching almost the size of the spray itself) and this effect leads to higher disturbance wavelength if compared to the previous zone.

Based on the analysis reported in [47, 48], some further analysis can be made on the type of atomization regime by studying the local Weber number We, defined as:

$$We = \frac{\rho u_r^2 D_l}{\sigma} \tag{16}$$

	λ/D_l	We
Red	10.9	3.2
Blue	7.9	5
Green	6	9

Table 3: Ligament parameters of the ligaments highlighted in Figure 10

where D_l is the ligament diameter (Figure 2) and u_r is the relative velocity between the liquid and the air, calculated as $u_r = u_l - u_g$, where the u_g is taken per each cell at a $1.5D_l$ from the ligament surface.

In order to analyse the axial evolution of the atomization process, three different ligament formation and breakup have been studied during their process, circled in Figure 10 in blue, red and green. Each one reflects different influences of the relative velocity field between liquid and air. In fact, it can be assumed that the farther the ligament is from the spray tip, the calmer will be the air, as it will show less influence from the tip larger eddy (effect (2) in section 4.1). This is testified by the decreasing Weber number along the spray axis: as the size of the 3 ligaments is comparable, is clear how the relative velocity between air and liquid is decreasing along the spray axis. Furthermore, is clear that most of the ligament velocity is generated by the spray liquid core, therefore this gives space to the conclusion that the relative velocity is higher in the spray region closer to the nozzle. The results shows a good agreement with the Weber numbers found for ligaments by [3].

Interesting conclusion can be drawn also on the secondary breakup and the formation of satellite droplets, based on the approach proposed in [47]. Being all the ligaments considered in this analysis in the medium wavelength Rayleigh breakup regime, this behaviour is assumed to be consistent and repeatable [47]. As reported in [47], the higher the ratio between the ligament wavelength λ and the ligament diameter D_l, the higher the ratio between the satellite droplet diameter and the main droplet diameter is. In other words, this indicates that, for sprays, secondary breakup is most likely to occur in regions where the Weber number is lower and therefore the air speed is higher.

4.5. Analysis of droplets generation

In order to assess the variation in the atomization process introduced by the synthetic inlet boundary condition, a study of the droplet statistics was performed. The study has been done over an average time of 20 μs when the spray has reached the complete penetration. Such a time interval is insufficient for turbulence statistics, but it provides a significant sample time for studying the droplet behaviour, as it allows the incoming spray to reach the end of the domain for case 1 and 2.

Figure 11(a) shows the droplet radius $d_v = \sqrt[3]{6V/\pi}$, where V is the droplet volume. The blue line shows the difference in number of droplets between case 2 and case 0, while the red line shows the difference

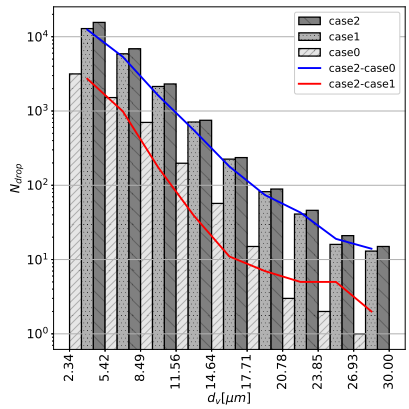

(a) Number of droplets against droplet diameter

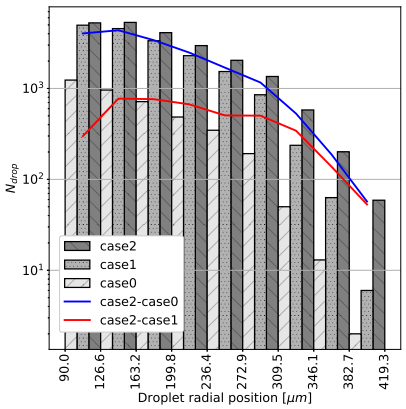

(b) Number of droplets against droplet radial position

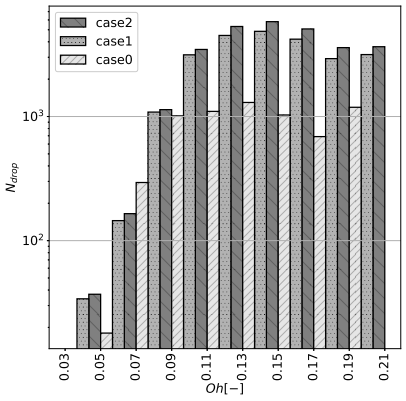

(c) Number of droplets against Oh number

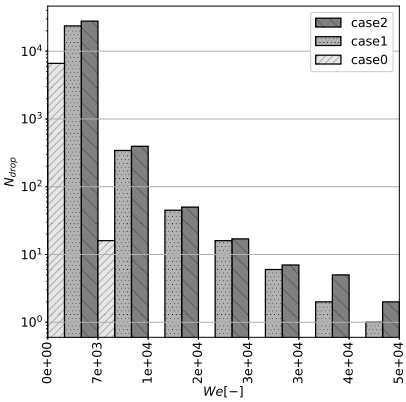

(d) Number of droplets against We number

Figure 11: Droplet statistics for the 3 cases.

between case 2 and case 1 (been case 2 the case with the largest number of broplets overall).In a first place, it is worth noting that, as already expressed in many works [49, 5], the droplets of a diameter smaller than two times the cell size should be neglected, as the VOF method is likely incapable to accurately describe the droplet of such a size. The number of droplets clearly decrease exponentially as the droplet diameter increase. It appears evidently that cases 1 and 2 generates a significant higher number of droplets, but no significant variation can be appreciated between this two cases. On the other hand, the difference between case 0 and cases 1 and 2 decrease almost exponentially. The difference between case 2 and 1 is almost negligible in respect to the total number of droplets in the 2 cases and it may be assumed that it is within the variability introduced by the random matrix generated for the synthetic boundary condition. Furthermore, is interesting to observe that case 1 and 2 also generates many liquid structures of significant size, showing that the instabilities generated by the synthetic boundary condition also allows the breakup of larger liquid structures (as it can be appreciated in Figure 10).

Figure 11(c) and 11(d) show respectively the Ohnesorge (Oh) and the Weber (We) number for the droplets. The Ohnesorge number is defined as:

$$Oh = \frac{\mu}{\sqrt{\rho \sigma d_v}} \tag{17}$$

It is important to notice that, in this case, the droplet velocity used for the We number determination in equation 16 is the absolute velocity of the droplet, being difficult to apply the previous criteria for the relative velocity u_r in the denser regions. Also, in this time average, there are no effects given by the tip vortices, therefore the faster droplets are likely to be located closer to the spray core. The higher number of droplet with a lower We number are representative of significant number of droplets with lower velocity and/or smaller size. These droplets are mostly the droplets that are stagnating in the peripheral area of the spray, where the spray cone angle is usually defined. As already said, for case 0 no spray axial breakup occur, therefore no spray cone angle can be defined. For this reason there are no droplets with higher We for case zero, meaning that the droplets detected are mostly in calm air regions and no new droplets (with higher kinetic energy) are formed in the time span where the analysis have been pursued. On the other hand, the Oh seems to behave in the same way for the three cases (as a consequence of a similar distribution for the droplet diameter) and highlights a general predominance of the viscous forces in respect of the surface tension forces.

Finally, Figure 11(b) shows the number of droplet and their radial distribution. Again, as for Figure 11(a) the blue and red lines are the difference in number of droplets as noted in the legend. For case 0 the number of droplet is decreasing faster as the radial position increase. This is a clear evidence that the droplets do not posses enough velocity to reach the domain borders, while case 1 and especially case 2 presents a high number of droplets at farther radius, implying a higher kinetic energy associated to each droplet. Figure 11(b) also allows to appreciate one of the biggest contribution introduced by the increment of the turbulence lengthscale. While the difference in the number of droplets between case 2 and 1 is relatively small at lower radius (less than one order of magnitude), it gets quite significant as the distance from the spray axis increase. This behaviour is quite significant as it is strictly related to the spray cone angle. In fact, experimental observations, made by means of Mie technique, identify the last region with a significant concentration of droplets as the region that defines the spray cone angle, that in this case would be significantly different for the three cases. As the spray cone angle observed in DNS simulations may be difficult to immediately compare with experimental data, these considerations will be useful guidelines for future studies.

4.6. Observation on gaussian behavior of the spray

As already seen in Figure 8, no axial breakup would be possible without simulating an appropriate turbulent boundary condition at the nozzle outlet. This process is fundamental in breaking the liquid core continuity. Furthermore, the turbulence inlet boundary condition is responsible for the axial velocity drop, causing the radial velocity to be distributed as a gaussian profile instead of top-hat profile.

As proved in [50, 32], a spray displays a gaussian behavior after a certain penetration. In other words, the dimensionless axial velocity (made dimensionless by dividing the temporal-averaged component U by the

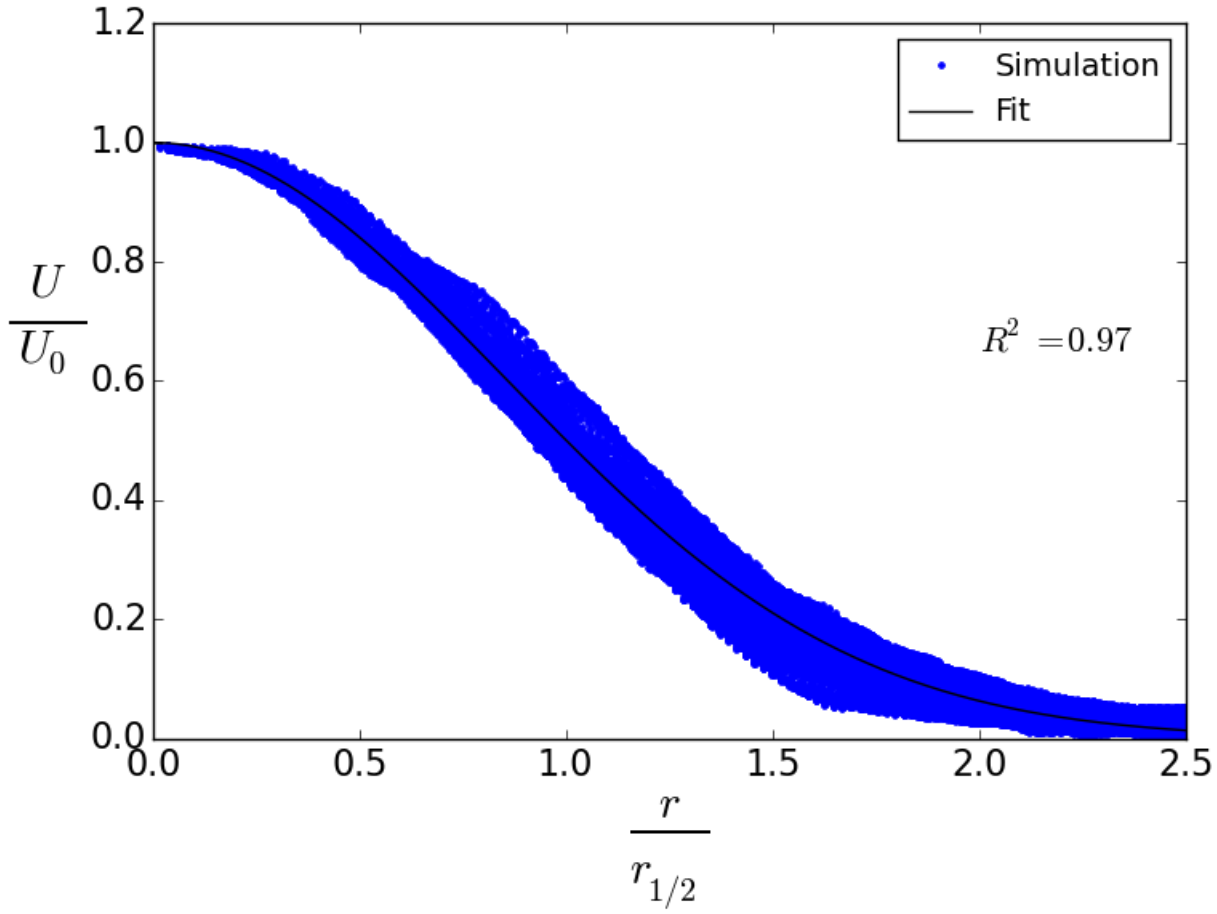

Figure 12: Self-similar profile obtained for case 1 at $x/D = 22$

centerline velocity U_0) drops with the same behaviour along the dimensionless radius (made dimensionless by dividing the radius r by the radial location at which the axial velocity drops by 50% in respect to the centerline velocity, $r_{1/2}$) at any axial position. More information about the axial velocity as a function of the density ratio between liquid and gas can be found at [17], that justify the applicability of the study in [50] to sprays. Figure 12 shows the gaussian profile obtained for case 1 at $x/D = 22$. The blue dots are the velocity values for all the points in that section, while the black line is the data interpolation, according to the following correlation

$$U(x,r) = U_0(x) \exp\left(-\alpha\left(\frac{r}{r_{1/2}}\right)\right) \tag{18}$$

provided in [17], where α is the coefficient for the gaussian radial profile, explained in [17]. This behaviour is obviously kept for each section at $x/D > 22$. The agreement between the simulation results and the expected behaviour can be assessed by the goodness of the fit. While the general behaviour is well captured, even better agreement is expected for higher wash-out time (time used by the fluid to get from the inlet to the outlet of the simulation domain), by increasing the simulation time. Due to the limitations in the domain size, dictated by the increasing computational costs, no other section can be displayed, because either to close to the outlet boundary, the non-gaussian region or to the section displayed.

As this behavior emerges clearly for case 1 and 2, it is clear how an inlet turbulent boundary condition is essential in order to reproduce the real behavior of the spray. Furthermore, the characterization of L and I, only achievable throughout simulation analysis, will be the object of future studies.

5. Conclusions

A synthetic boundary condition for turbulence has been implemented in the open source code Paris-Simulator and has been used to study primary atomization at different levels of turbulence, quantified by its lengthscale L and its intensity I. The effects of the nozzle perturbation have been analyzed both through its influence on the velocity distribution, as well as by typical engineering parameters such as *external non-perturbed length* and *intact core length*.

As largely discussed in section 4, the turbulence generated inside the nozzle affects heavily the atomization process, by deforming the spray shape and increasing the level of vorticity close to the spray core and to the *atomized region*.

Finally, for the case that shows a more realistic behavior (case 2), analysis on the causes for local atomization process have been made, focusing on the how the local velocity fluctuation influence the size of ligaments and liquid structures.

This study shows how internal nozzle flows affect the spray formation as well as the local atomization. For this reason, future studies will be done on the nozzle internal flow in order to characterize the turbulence field generated inside the nozzle.

6. Acknowledgment

This work was partly sponsored by "Ministerio de Economía y Competitividad", of the Spanish Government, in the frame of the Project "Estudio de la interacción chorro-pared en condiciones realistas de motor", Reference TRA2015-67679-c2-1-R. The author thankfully acknowledges the computer resources at MareNostrum (BSC) and the technical support provided by FI-2016-3-0031.

References

[1] A. H. Lefèbvre, Atomization and Sprays, CRC, 1989.
[2] J. B. Heywood, Internal Combustion Engine Fundementals, Vol. 21, 1988.
[3] J. Shinjo, A. Umemura, Simulation of liquid jet primary breakup: Dynamics of ligament and droplet formation, International Journal of Multiphase Flow 36 (7) (2010) 513–532. doi:10.1016/j.ijmultiphaseflow.2010.03.008.
URL http://linkinghub.elsevier.com/retrieve/pii/S0301932210000637

[4] Y. Ling, S. Zaleski, R. Scardovelli, Multiscale simulation of atomization with small droplets represented by a Lagrangian point-particle model, International Journal of Multiphase Flow 76 (2015) 122–143. doi:10.1016/j.ijmultiphaseflow.2015.07.002.
URL http://www.sciencedirect.com/science/article/pii/S0301932215001524

[5] Y. Ling, D. Fuster, S. Zaleski, G. Tryggvason, Spray formation in a quasiplanar gas-liquid mixing layer at moderate density ratios: A numerical closeup, Physical Review Fluids 2 (1) (2017) 014005. doi:10.1103/PhysRevFluids.2.014005.
URL https://link.aps.org/doi/10.1103/PhysRevFluids.2.014005

[6] R. Lebas, T. Menard, P. Beau, A. Berlemont, F. Demoulin, Numerical simulation of primary break-up and atomization: DNS and modelling study 35 (3) (2009) 247–260. doi:10.1016/j.ijmultiphaseflow.2008.11.005.
URL http://linkinghub.elsevier.com/retrieve/pii/S0301932208001821http://www.sciencedirect.com/science/article/pii/S0301932208001821

[7] F. Payri, V. Bermúdez, R. Payri, F. J. Salvador, The influence of cavitation on the internal flow and the spray characteristics in diesel injection nozzles, Fuel 83 (4-5) (2004) 419–431. doi:10.1016/j.fuel.2003.09.010.
URL http://www.sciencedirect.com/science/article/B6V3B-49S6P9B-1/2/9f0f82ab914af7a5db32ee0c133d7e7d

[8] F. J. Salvador, J. Martínez-López, J. V. Romero, M. D. Roselló, Computational study of the cavitation phenomenon and its interaction with the turbulence developed in diesel injector nozzles by Large Eddy Simulation (LES), Mathematical and Computer Modelling 57 (7-8) (2013) 1656–1662. doi:10.1016/j.mcm.2011.10.050.
URL http://dx.doi.org/10.1016/j.mcm.2011.10.050

[9] N. Mitroglou, M. McLorn, M. Gavaises, C. Soteriou, M. Winterbourne, Instantaneous and ensemble average cavitation structures in Diesel micro-channel flow orifices, Fuel 116 (2014) 736–742. doi:10.1016/j.fuel.2013.08.060.
URL http://dx.doi.org/10.1016/j.fuel.2013.08.060

[10] F. J. Salvador, S. Hoyas, R. Novella, J. Martínez-López, Numerical simulation and extended validation of two-phase compressible flow in diesel injector nozzles, Proceedings of the Institution of Mechanical Engineers, Part D: Journal of Automobile Engineering 225 (4) (2011) 545–563. doi:10.1177/09544070JAUTO1569.

[11] S. Molina, F. J. Salvador, M. Carreres, D. Jaramillo, A computational investigation on the influence of the use of elliptical orifices on the inner nozzle flow and cavitation development in diesel injector nozzles, Energy Conversion and Management 79 (2014) 114–127. doi:10.1016/j.enconman.2013.12.015.
URL http://linkinghub.elsevier.com/retrieve/pii/S0196890413007917

[12] B. Yin, S. Yu, H. Jia, J. Yu, Numerical research of diesel spray and atomization coupled cavitation by Large Eddy Simulation (LES) under high injection pressure, International Journal of Heat and Fluid Flow 59 (2016) 1–9. doi:10.1016/j.ijheatfluidflow.2016.01.005.

[13] J. J. Lopez, F. J. Salvador, O. A. De la Garza, J. Arrègle, A comprehensive study on the effect of cavitation on injection velocity in diesel nozzles, Energy Conversion and Management 64 (2012) 415–423. doi:10.1016/j.enconman.2012.03.032.

[14] R. Payri, F. J. Salvador, J. Gimeno, R. Novella, Flow regime effects on non-cavitating injection nozzles over spray behavior, International Journal of Heat and Fluid Flow 32 (1) (2010) 273–284.
URL http://www.sciencedirect.com/science/article/pii/S0142727X10001633

[15] J. M. Lujan, B. Tormos, F. J. Salvador, K. Gargar, Comparative analysis of a DI diesel engine fuelled with biodiesel blends during the European MVEG-A cycle: Preliminary study (I), Biomass and Bioenergy 33 (6-7) (2009) 941–947. doi:10.1016/j.biombioe.2009.02.004.
URL http://linkinghub.elsevier.com/retrieve/pii/S0961953409000403

[16] F. J. Salvador, S. Ruiz, J. Gimeno, J. De la Morena, Estimation of a suitable Schmidt number range in diesel sprays at high injection pressure, International Journal of Thermal Sciences 50 (9) (2011) 1790–1798. doi:10.1016/j.ijthermalsci.2011.03.030.
URL http://linkinghub.elsevier.com/retrieve/pii/S1290072911001165

[17] J. M. Desantes, F. J. Salvador, J. J. Lopez, J. De la Morena, Study of mass and momentum transfer in diesel sprays based on X-ray mass distribution measurements and on a theoretical derivation, Experiments in Fluids 50 (2) (2011) 233–246. doi:10.1007/s00348-010-0919-8.
URL http://link.springer.com/article/10.1007/s00348-010-0919-8

[18] F. J. Salvador, J. V. Romero, M. D. Roselló, D. Jaramillo, Journal of Computational and Applied Mathematicsdoi:10.1016/j.cam.2015.03.044.

[19] M. Klein, A. Sadiki, J. Janicka, A digital filter based generation of inflow data for spatially developing direct numerical or large eddy simulations, Journal of Computational Physics 186 (2) (2003) 652–665. doi:10.1016/S0021-9991(03)00090-1.

[20] J. HŒPFFNER, Y. NAKA, K. FUKAGATA, Realizing turbulent statistics, Journal of Fluid Mechanics 676 (2011) 54–80. doi:10.1017/jfm.2011.32.
URL http://www.journals.cambridge.org/abstract{_}S0022112011000322

[21] L. Perret, J. Delville, R. Manceau, J. P. Bonnet, Turbulent inflow conditions for large-eddy simulation based on low-order empirical model, Physics of Fluids 20 (7). doi:10.1063/1.2957019.

[22] S. Lee, S. K. Lele, P. Moin, Simulation of spatially evolving turbulence and the applicability of Taylor's hypothesis in compressible flow, Physics of Fluids A: Fluid Dynamics 4 (7) (1992) 1521–1530. doi:10.1063/1.858425.
URL http://aip.scitation.org/doi/10.1063/1.858425

[23] P. Sagaut, Large eddy simulation for incompressible flows: an introduction, Springer Science & Business Media, 2006.

[24] G. R. Tabor, M. H. Baba-Ahmadi, Inlet conditions for large eddy simulation: A review, Computers & Fluids 39 (4) (2010) 553–567. doi:10.1016/j.compfluid.2009.10.007.
URL http://dx.doi.org/10.1016/j.compfluid.2009.10.007

[25] P. Druault, S. Lardeau, J.-P. Bonnet, F. Coiffet, J. Delville, E. Lamballais, J.-F. Largeau, L. Perret, Generation of

Three-Dimensional Turbulent Inlet Conditions for Large-Eddy Simulation, AIAA Journal 42 (3) (2004) 447–456. doi:10.2514/1.3946.

[26] D. Jarrahbashi, W. A. Sirignano, P. P. Popov, F. Hussain, Early spray development at high gas density: hole, ligament and bridge formations, Journal of Fluid Mechanics 792 (2016) 186–231. doi:10.1017/jfm.2016.71.
URL http://www.journals.cambridge.org/abstract{_}S0022112016000719

[27] G. Agbaglah, S. Delaux, D. Fuster, J. Hoepffner, C. Josserand, S. Popinet, P. Ray, R. Scardovelli, S. Zaleski, Parallel simulation of multiphase flows using octree adaptivity and the volume-of-fluid method, Comptes Rendus Mécanique 339 (2-3) (2011) 194–207. doi:10.1016/j.crme.2010.12.006.
URL http://www.sciencedirect.com/science/article/pii/S1631072110002160

[28] G. Tryggvason, R. Scardovelli, S. Zaleski, Direct numerical simulations of gas–liquid multiphase flows, Cambridge University Press, 2011.

[29] A. J. Chorin, Numerical solution of the Navier-Stokes equations, Mathematics of Computation 22 (1968) 745–762. doi:10.2307/2004575.

[30] B. P. Leonard, A stable and accurate convective modelling procedure based on quadratic upstream interpolation, Computer methods in applied mechanics and engineering 19 (1) (1979) 59–98.

[31] R. Scardovelli, S. Zaleski, Direct Numerical Simulation of Free-Surface and Interfacial Flow, Annual Review of Fluid Mechanics 31 (1) (1999) 567–603. doi:10.1146/annurev.fluid.31.1.567.

[32] S. Pope, Turbulent Flows, sixth Edition, Cambridge University Press, 2009.

[33] T. S. Lund, X. Wu, K. D. Squires, Generation of turbulent inflow data for spatially-developing boundary layer simulations, J. Comp. Phys. 140 (1998) 233–258.

[34] G. K. Batchelor, The theory of homogeneous turbulence, Cambridge university press, 1953.

[35] J. G. M. Eggels, F. Unger, M. H. Weiss, J. Westerweel, R. J. Adrian, R. Friedrich, F. T. M. Nieuwstadt, Fully developed turbulent pipe flow: a comparison between direct numerical simulation and experiment, Journal of Fluid Mechanics 268 (-1) (2006) 175. doi:10.1017/S002211209400131X.
URL http://www.journals.cambridge.org/abstract{_}S002211209400131X

[36] G. K. El Khoury, P. Schlatter, A. Noorani, P. F. Fischer, G. Brethouwer, A. V. Johansson, Direct numerical simulation of turbulent pipe flow at moderately high reynolds numbers, Flow, Turbulence and Combustion 91 (3) (2013) 475–495. doi:10.1007/s10494-013-9482-8.

[37] J. Benajes, F. J. Salvador, M. Carreres, D. Jaramillo, On the relation between the external structure and the internal characteristics in the near-nozzle field of diesel sprays, Proceedings of the Institution of Mechanical Engineers, Part D: Journal of Automobile Engineeringdoi:10.1177/0954407016639464.

[38] M. Ghiji, L. Goldsworthy, P. Brandner, V. Garaniya, P. Hield, Numerical and experimental investigation of early stage diesel sprays, Fuel 175 (2016) 274–286. doi:10.1016/j.fuel.2016.02.040.
URL http://www.sciencedirect.com/science/article/pii/S0016236116001617

[39] J. Hult, P. Simmank, S. Matlok, S. Mayer, Z. Falgout, M. Linne, Interior flow and near-nozzle spray development in a marine-engine diesel fuel injector, Experiments in Fluids 57 (4) (2016) 49. doi:10.1007/s00348-016-2134-8.
URL http://link.springer.com/10.1007/s00348-016-2134-8

[40] R. Payri, F. J. Salvador, J. Gimeno, J. De la Morena, Analysis of Diesel spray atomization by means of a near-nozzle field visualization technique, Atomization and Sprays 21 (9) (2011) 753–774. doi:10.1615/AtomizSpr.2012004051.

[41] L. M. Pickett, C. L. Genzale, G. Bruneaux, L.-M. Malbec, C. Christiansen, Comparison of diesel spray combustion in different high-temperature, high-pressure facilities, SAE Int. J. Engines 3 (2010) 156–181. doi:10.4271/2010-01-2106.

[42] S. Bnà, S. Manservisi, R. Scardovelli, P. Yecko, S. Zaleski, Vofi — A library to initialize the volume fraction scalar field, Computer Physics Communications 200 (2015) 291–299. doi:10.1016/j.cpc.2015.10.026.
URL http://linkinghub.elsevier.com/retrieve/pii/S0010465515004087

[43] J. Shinjo, J. Xia, a. Umemura, Droplet/ligament modulation of local small-scale turbulence and scalar mixing in a dense fuel spray, Proceedings of the Combustion Institute 35 (2) (2015) 1595–1602. doi:10.1016/j.proci.2014.06.088.
URL http://linkinghub.elsevier.com/retrieve/pii/S1540748914002466

[44] T. Ménard, S. Tanguy, A. Berlemont, Coupling level set/VOF/ghost fluid methods: Validation and application to 3D simulation of the primary break-up of a liquid jet, International Journal of Multiphase Flow 33 (5) (2007) 510–524. doi:10.1016/j.ijmultiphaseflow.2006.11.001.
URL http://www.sciencedirect.com/science/article/pii/S0301932206001832

[45] D. Jarrahbashi, W. A. Sirignano, Invited Article: Vorticity dynamics for transient high-pressure liquid injection, Physics of Fluids 26 (10). doi:10.1063/1.4895781.
URL http://dx.doi.org/10.1063/1.4895781

[46] R. Payri, G. Bracho, P. Marti-Aldaravi, A. Viera, Near field visualization of diesel spray for different nozzle inclination angles in non-vaporizing conditions., Atomization and Sprays (accepted reference AAS-17949).

[47] P. Vassallo, N. Ashgriz, Satellite Formation and Merging in Liquid Jet Breakup, Proceedings of the Royal Society A: Mathematical, Physical and Engineering Sciences 433 (1888) (1991) 269–286. doi:10.1098/rspa.1991.0047.
URL http://rspa.royalsocietypublishing.org/content/433/1888/269.abstract

[48] N. Ashgriz, Handbook of atomization and sprays: theory and applications, Springer Science & Business Media, 2011.

[49] J. Shinjo, a. Umemura, Detailed simulation of primary atomization mechanisms in Diesel jet sprays (isolated identification of liquid jet tip effects), Proceedings of the Combustion Institute 33 (2) (2011) 2089–2097. doi:10.1016/j.proci.2010.07.006.
URL http://linkinghub.elsevier.com/retrieve/pii/S154074891000235Xhttp://dx.doi.org/10.1016/j.proci.2010.07.006

[50] H. J. Hussein, S. P. Capp, W. K. George, Velocity measurements in a high-Reynolds-number, momentum-conserving, axisymmetric, turbulent jet, Journal of Fluid Mechanics 258 (1994) 31–75.